nature physics

ARTICLES

PUBLISHED ONLINE: 11 NOVEMBER 2012 | DOI: 10.1038/NPHYS2479

Zero-bias peaks and splitting in an Al–InAs nanowire topological superconductor as a signature of Majorana fermions

Anindya Das†, Yuval Ronen†, Yonatan Most, Yuval Oreg, Moty Heiblum* and Hadas Shtrikman

Majorana fermions are the only fermionic particles that are expected to be their own antiparticles. Although elementary particles of the Majorana type have not been identified yet, quasi-particles with Majorana-like properties, born from interacting electrons in the solid, have been predicted to exist. Here, we present thorough experimental studies, backed by numerical simulations, of a system composed of an aluminium superconductor in proximity to an indium arsenide nanowire, with the latter possessing strong spin–orbit coupling and Zeeman splitting. An induced one-dimensional topological superconductor, supporting Majorana fermions at both ends, is expected to form. We concentrate on the characteristics of a distinct zero-bias conductance peak and its splitting in energy—both appearing only with a small magnetic field applied along the wire. The zero-bias conductance peak was found to be robustly tied to the Fermi energy over a wide range of system parameters. Although not providing definite proof of a Majorana state, the presented data and the simulations support its existence.

Quantum mechanics and special relativity were merged into a single theory when Dirac presented his equation in 1929[1], with a solution predicting an electron and an anti-electron partner—the positron. Majorana, however, showed that Dirac's equation also has real solutions—the so-called Majorana fermions[2], which are their own anti-particles[3]. In condensed-matter physics, the Majorana fermion is an emergent quasi-particle zero-energy state[4,5]. The fundamental aspects of Majoranas and their non-Abelian braiding properties[6,7] offer possible applications in quantum computation[8–10]. Examples of leading candidates to host Majoranas are: Moore–Read-type states in the fractional quantum Hall effect[11]; vortices in two-dimensional (2D) $p+ip$ spinless superconductors[12]; and domain walls in 1D p-wave superconductors[4,13]. As conventional s-wave superconductors are more easily implemented than p-wave ones, several suggestions for their implementations have recently been proposed: the surface of a 3D topological insulator in proximity to an s-wave superconductor[14]; a 2D semiconductor with strong spin–orbit coupling in proximity to an s-wave superconductor under broken time reversal symmetry (using a local ferromagnet[15,16] or an external magnetic field[17]); and a 1D semiconductor with the Majorana quasi-particles appearing at the two ends of the 1D wire[4,5,18,19]. Specifically, the authors of refs 18,19 proposed to employ InAs or InSb nanowires, possessing strong spin–orbit coupling and large Zeeman splitting at low magnetic fields, in proximity to an s-wave superconductor. Following the suggestion of ref. 19 to use an InSb nanowire, recent reports[20,21] demonstrated the observation of a magnetic-field-induced zero-bias conductance peak (ZBP), as expected for a zero-energy Majorana state.

Here, we report the observation of a ZBP and its splitting under different conditions of magnetic field, chemical potential and temperature, in a high-quality suspended InAs nanowire in proximity to an Al superconductor. We compare the experimental results with numerical simulations based on scattering theory and find, using the experimental parameters, a qualitative agreement of the data with a Majorana state. We also discuss alternative models that may account for the observed ZBP (refs 22–24).

Theoretical aspects of Majorana states

As our main goal is to find evidence of the formation of Majorana states, it is important to specify the required conditions for their formation. The most basic requirement is that the quasi-particle is spinless. These requirements can be satisfied by p-wave Cooper pairing of spinless particles[5], or in $\nu+(1/2)$ filling factor (where ν is an integer) in the fractional quantum Hall effect[11]. Here we present a realization of a 1D nanowire coupled to an s-wave superconductor, thus, with an induced superconductivity. Rashba spin–orbit coupling[25], leading to an effective magnetic field $\mathbf{B}_{so} \propto \mathbf{p}\times\mathbf{E}$ (where $\mathbf{p}$ is the momentum along the wire and $\mathbf{E}$ is the electric field perpendicular to the wire), separates electrons with opposite spins in momentum space. Applying a magnetic field perpendicular to $\mathbf{B}_{so}$ will mix the two spin bands, forming two pseudo-spin bands, Zeeman gapped by $2E_Z$ at $p=0$ (Fig. 1a,b). Inducing superconductivity modifies the Zeeman gap at $p=0$ and opens up a gap at the Fermi momentum p_F (Fig. 1c). The overall gap E_g is the smaller of these two gaps. Three parameters are of significance: the spin–orbit energy $\Delta_{so}=p_{so}^2/2m$, with $\pm p_{so}=\pm\hbar/\lambda_{so}$ (Fig. 1a); the Zeeman gap $2E_Z=g\mu_B B$, where g is the Landé g-factor, μ_B is the Bohr magnetron and B is the external magnetic field; and the induced superconducting gap in the nanowire $2\Delta_{ind}$ (the Al superconducting gap is $2\Delta_{Al}$). For $\Delta_{ind}>0$ and $E_Z=0$ the wire is a trivial superconductor with a gapped spectrum. When E_Z is increased to $E_Z=\sqrt{\Delta_{ind}^2+\mu^2}$, where μ is the chemical potential (Fig. 1a), the gap at $p=0$ closes at the Fermi energy, and the wire enters the topological phase; with a topological gap reopening with a further increase in E_Z. Continuously changing the parameters along the wire from its topological phase into another gapped phase must close the gap at the phase transition point, forming a Majorana

Braun Center for Submicron Research, Department of Condensed Matter Physics, Weizmann Institute of Science, Rehovot 76100, Israel. †These authors contributed equally to this work. *e-mail: moty.heiblum@weizmann.ac.il.

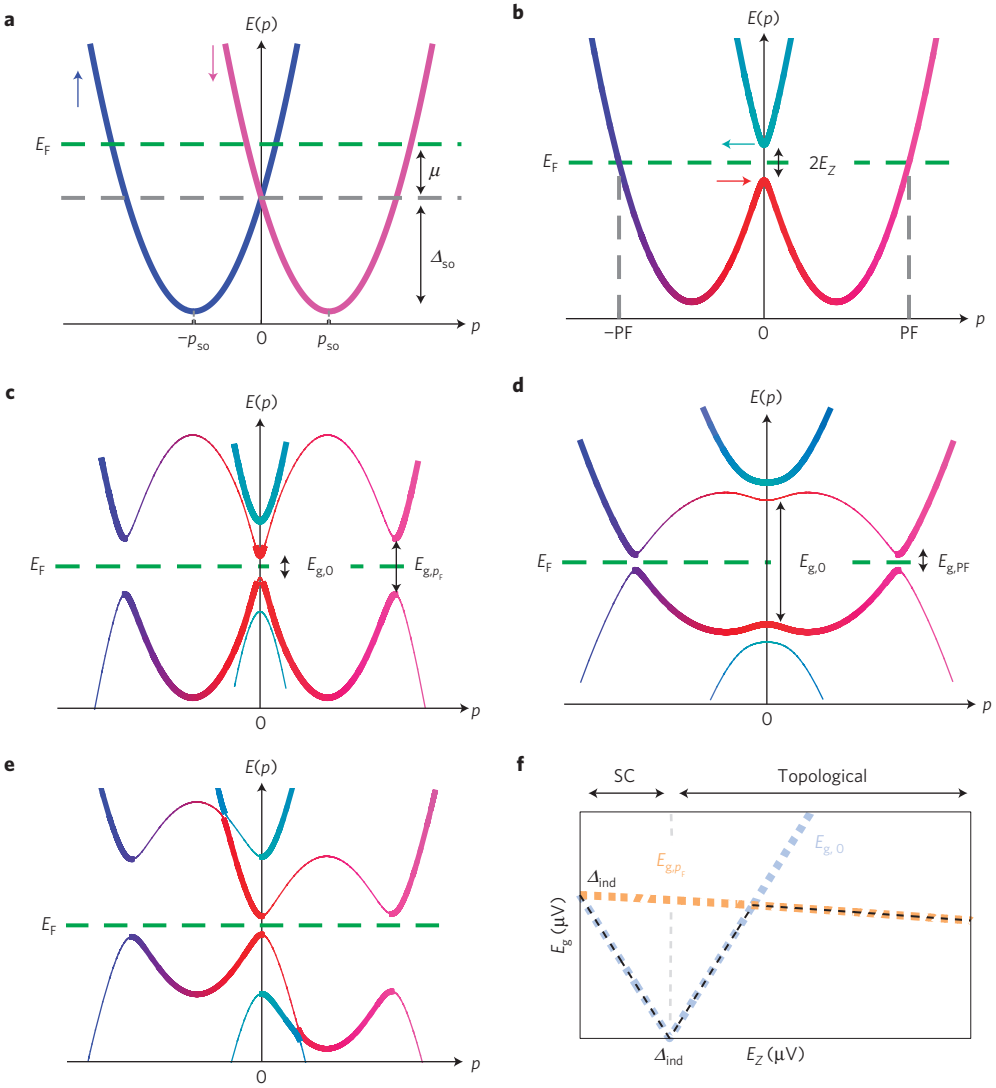

Figure 1 | Energy dispersion of InAs nanowire excitations (Bogoliubov–de Gennes spectrum), in proximity to an Al superconductor. Heavy (light) lines show electron-like (hole-like) bands. Opposite spin directions are denoted in blue and magenta for the spin–orbit effective field direction; red and cyan for the spins in the perpendicular direction; relative mixture denotes intermediate spin directions. **a**, Split electronic spin bands due to spin–orbit coupling. The spin–orbit energy is denoted as Δ_{so}; the chemical potential is μ, with respect to spin bands crossing at $p=0$. **b**, With applied magnetic field $B\perp B_{so}$, leading to a Zeeman gap $E_Z=1/2g\mu_B B$ at $p=0$. **c**, Bringing a superconductor into close proximity opens a superconducting gap at the crossing of particle and hole curves (light lines). **d**, The same as in **c** but for a larger E_Z with the gap at p_F dominant. **e**, Field rotated to a direction of 30° with respect to B_{so}, leading to shifts of the original spin–orbit bands. **f**, The evolution of the energy gap at $p=0$ (dotted blue), at p_F (dotted yellow), and the overall energy gap (dashed black) with Zeeman energy, E_Z, for $\mu=0$.

state. Another quasi-particle state is formed at the other end of the topological segment[4].

The required condition for a topological superconductor is therefore $E_Z > \sqrt{\Delta_{ind}^2+\mu^2}$ (or equivalently $E_Z > \Delta_{ind}$ and $|\mu| < \sqrt{E_Z^2-\Delta_{ind}^2}$). For Zeeman energies close to the topological phase transition, the smaller gap is at $p=0: E_g=2|E_Z-\sqrt{\Delta_{ind}^2+\mu^2}|$ (Fig. 1f). For larger Zeeman energies, the gap at p_F is the smaller of the two, which for $E_Z \gg \Delta_{so}$, Δ_{ind}, $|\mu|$ is given by $E_g=4\Delta_{ind}\sqrt{\Delta_{so}/E_Z}$ (Fig. 1f). In this regime the gap decreases with E_Z, and even more so owing to the diminishing of the superconducting gap with field. The Majoranas, with energy ε pinned to the Fermi energy, should be robust for a range of system parameters that keep $|\mu| < \sqrt{E_Z^2-\Delta_{ind}^2}$. The immediate consequence of the Majorana is a sharp enhancement in the tunnelling density of states and a $2e^2/h$ differential conductance at zero applied bias and $T=0$ (refs 26,27; the actual width and height of the peak are determined by the relation of the barrier height to the electron temperature, and the coupling between the two Majoranas at the ends of the topological segment). Here we aim to perform multiple experiments with a set of results that favour the Majorana states on other possible states.

Set-up of devices

InAs wires were chosen owing to the lack of a Schottky barrier to a metallic electrode and the strong spin–orbit coupling and Zeeman splitting of the electrons. A scanning electron micrograph of our device, as well as its schematic illustration, is shown in Fig. 2. Wurtzite InAs nanowires of 50–60 nm in diameter and free of stacking faults were grown by Au-assisted vapour-liquid–solid molecular beam epitaxy on (011) InAs substrate (after oxide blow off and *in situ* evaporation of a thin gold layer in a separated vacuum connected chamber)[28]. A typical high-resolution transmission electron microscopy (TEM) image taken from such a nanowire is shown in the inset of Fig. 2 (see also Supplementary Fig. S3). The nanowires were suspended on a gold pillar at each

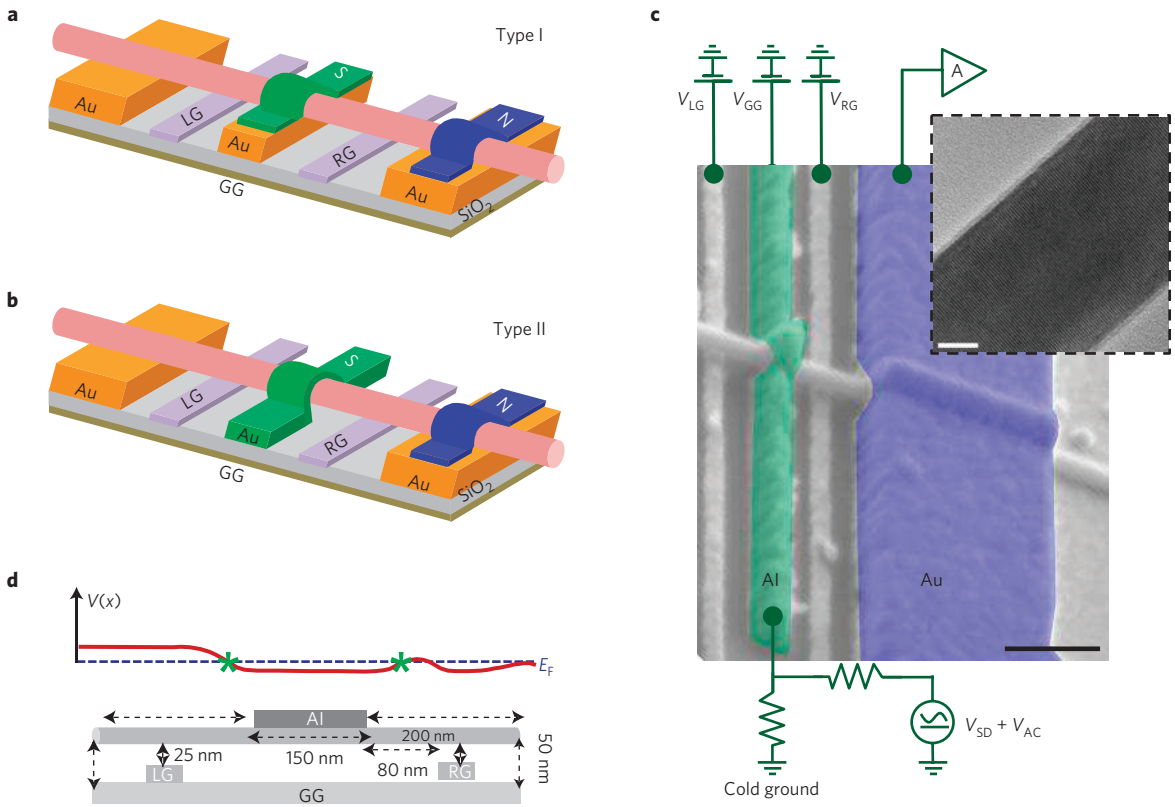

Figure 2 | A suspended Al–InAs nanowire on gold pedestals above p-type silicon. The p-type silicon serves as a global gate (GG) coated with 150 nm SiO_2. **a**, A type I device with an additional gold pedestal at the centre, a gold normal contact at each end of the wire and an aluminium superconducting contact at the centre. Two narrow local gates (RG and LG), 50 nm wide and 25 nm high, displaced from the superconducting contact by 80 nm, affect both the barrier height near the Al edge and the chemical potential in the wire. **b**, A type II device without the centre pedestal, thus allowing control of the chemical potential under the Al contact. **c**, Scanning electron micrograph of a type II device (scale bar, 300 nm), with a 5 Ω voltage source V_{SD} and a cold-grounded drain. Inset: high-resolution TEM image (viewed from the ⟨1120⟩ zone axis) of a stacking-fault-free, wurtzite-structure, InAs nanowire, grown on (011) InAs in the ⟨111⟩ direction. The TEM image (scale bar, 10 nm) is courtesy of R. Popovitz-Biro. A more detailed image can be found in the Supplementary Information. **d**, An estimated potential profile along the wire.

end, some 50 nm above a Si/SiO_2 substrate. Two types of device were tested (Fig. 2a,b): in both, the wires were contacted with two gold layers at their ends (serving as low-resistance contacts), and a superconducting aluminium strip (100 nm thick and ∼150 nm wide) at the centre. In type I devices a gold pillar supported the wire under the aluminium electrode (the Al critical field was ∼60–70 mT), whereas in type II devices the centre pillar was missing (the Al critical field was ∼100–150 mT for different devices) and the critical temperature was ∼1 K, consistent with the superconducting Bardeen–Cooper–Schrieffer gap ($\Delta \sim 150\,\mu eV$). The conducting Si substrate served as a global gate (effective under the superconductor only in type II devices), and two additional narrow local gates (Fig. 2d), placed 80 nm away from the superconductor edges (25 nm thick, 50 nm wide). Being close to the wire, they affected both the potential barriers near the edges of the superconductor, and the chemical potential along the wire.

Before cooling, the devices dwelled at room temperature in a vacuum pumped chamber for 24 h with the conductance increasing by some 20-fold (owing to desorption of surface impurities). With the dilution refrigerator temperature at 10 mK, the estimated electron temperature in the wire was ∼30 mK. A 575 Hz 1–2 μV root-mean-squared signal was fed to the superconducting contact and the resultant current was collected at one side of the wire (by the ohmic contact), to be amplified later by a home-made current amplifier (Fig. 2). We also measured the conductance at a higher frequency (∼1 MHz), employing a low-noise voltage preamplifier cooled to 1 K (ref. 29).

Our numerical simulations were based on a generalization of the formalism pioneered by Blonder, Tinkham and Klapwijk[30], which allows modelling a large number of segments in the wire, including spin flip processes, going beyond the small bias approximation. Each segment was characterized by different parameters, with discontinuous jumps at the interfaces. Using wavefunctions matching at the interfaces, the Bogoliubov–de Gennes equations were solved to find the scattering states at each energy and thus the corresponding transmission and reflection amplitudes (for further details see, the Supplementary Information and refs 31–34).

Study of the parameters

We start with a calibration of the two types of studied device. Bare and ungated wires are n-type with a density of $\sim 10^6\ cm^{-1}$, and thus are likely to occupy a single subband. The presence of disorder and weak barriers near the metal contacts make the conductance highly sensitive to the chemical potential, namely, to the gate voltage. At the lower conductance range (large barrier at the superconductor interface, or low density), Cooper pair transport is suppressed and the zero-bias conductance may be flat or exhibit either dips or peaks. There are a few potential causes of the observed ZBPs; reflectionless tunnelling, being constructive interference between electron reflection and Andreev reflection[35] in S–I–N–I devices (I, insulator; S, superconductor; N, normal), which are expected to quench with magnetic field[36,37]; Andreev bound state—common in S–N–I, likely to be split (weakly) at zero field and Zeeman split further with field[38,39]; Kondo correlations—due to weakly confined

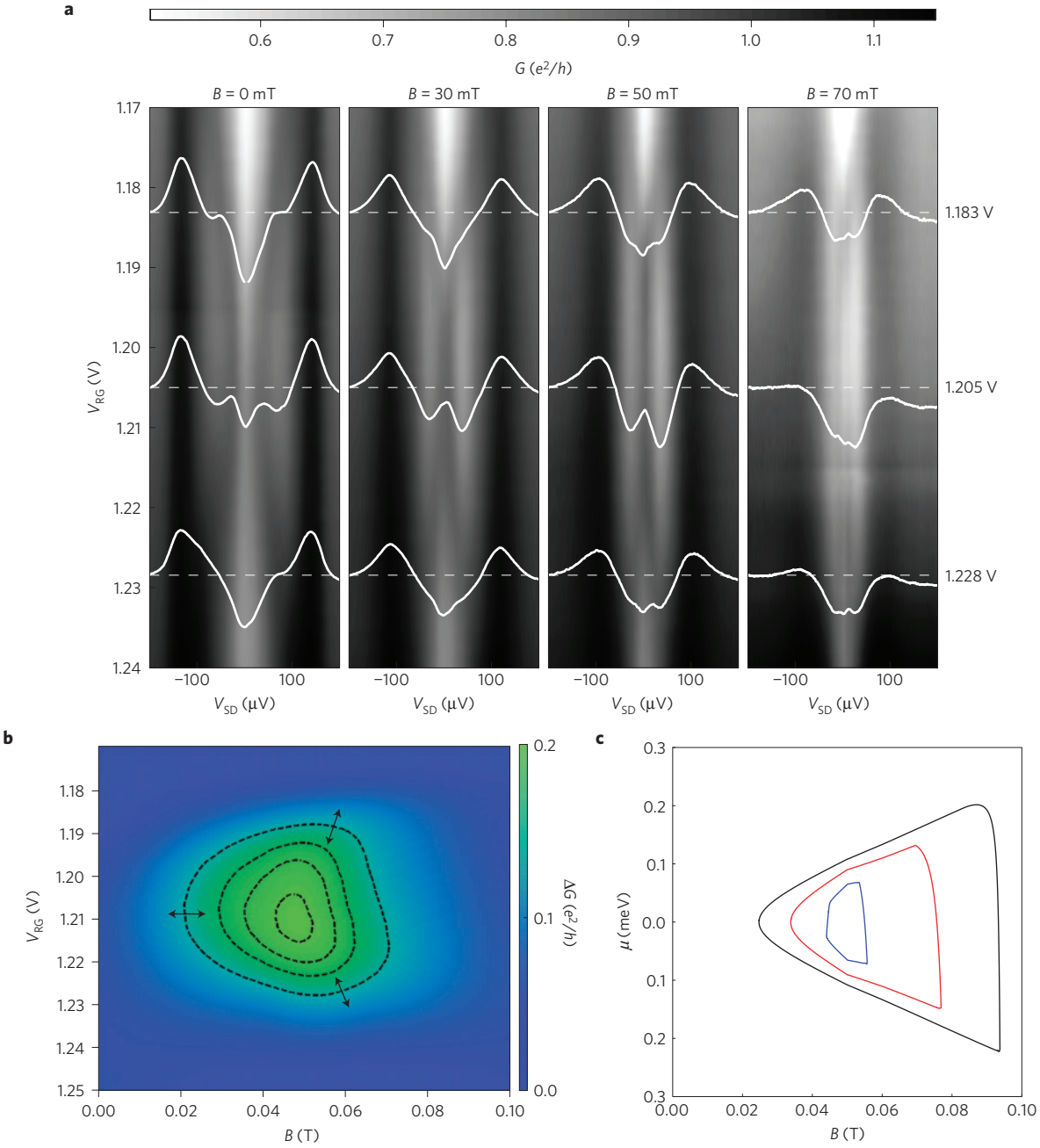

Figure 3 | Evolution of the ZBP with chemical potential and magnetic field, for the V_{RG} range 1.17–1.24 V at $V_{GG} = -18.3$ V for a type II device (D4). The cuts are taken at $V_{RG} = 1.183$, 1.205 and 1.228 V. **a**, The main features at $B = 0$ are the Al superconducting gap $\Delta_{Al} \sim \pm 150$ μeV, and the induced gap $\Delta_{ind} \sim \pm 45$ μeV. At $B = 30$ mT the gap closes at $V_{RG} = 1.205$ V and turns into a relatively wide, barely split, ZBP; to split at higher and lower gate voltages. At $B = 50$ mT, a sharper ZBP persists in a wide range of gate voltage, with marked splitting. At $B = 70$ mT, the ZBP peak splits in a wide range of gate voltage. **b**, Colour plot of the ZBP with equal height contours lines, from $0.106e^2/h$ to $0.197e^2/h$. The arrows indicate the transition from a single ZBP to split peaks. **c**, Simulated behaviour using analytical expressions for the wire spectrum. Contours lines of constant-size Majorana wavefunction, $\xi = \hbar v_F/E_g \sim 1.5\,L$, 3L and 10L are blue, red and black, respectively. The simulation of $\xi < 3L$ (red line contour) is similar to the contours of the data **b**. Although the range of chemical potential for which the wire is topological increases as a function of B, at higher B the gap decreases, increasing the extent of the Majoranas. The sharp termination of each contour at some maximal value of B is due to the weak dependence of Δ_{ind} on μ.

electron puddle(s) between the topological or the bare wire segments. Being pronounced at small or vanishing superconducting gap, and exhibiting Zeeman splitting[40,41]; weak anti-localization, which may be pronounced with field, but is more likely in a multiple channel device[42]. These plausible effects will be addressed in the discussion section and in the Supplementary Information.

From the observed Zeeman splitting of the zero-field ZBP, we estimated $g \sim 20$ (we assumed an equal voltage drop on the two inadvertent potential barriers—one at the superconductor/normal interface and one and at the ohmic contact/normal interface, leading to $4E_Z \cong 125$ μeV at $B = 50$ mT; ref. 43). The apparently large g-factor may represent an enhanced magnetic field along the wire due to its repulsion from the bulk of the superconductor.

Most of the presented data were taken with type II devices. Two main features were always observed in the conductance as a function of eV_{SD} (see Figs 3–5). The first feature is two symmetric

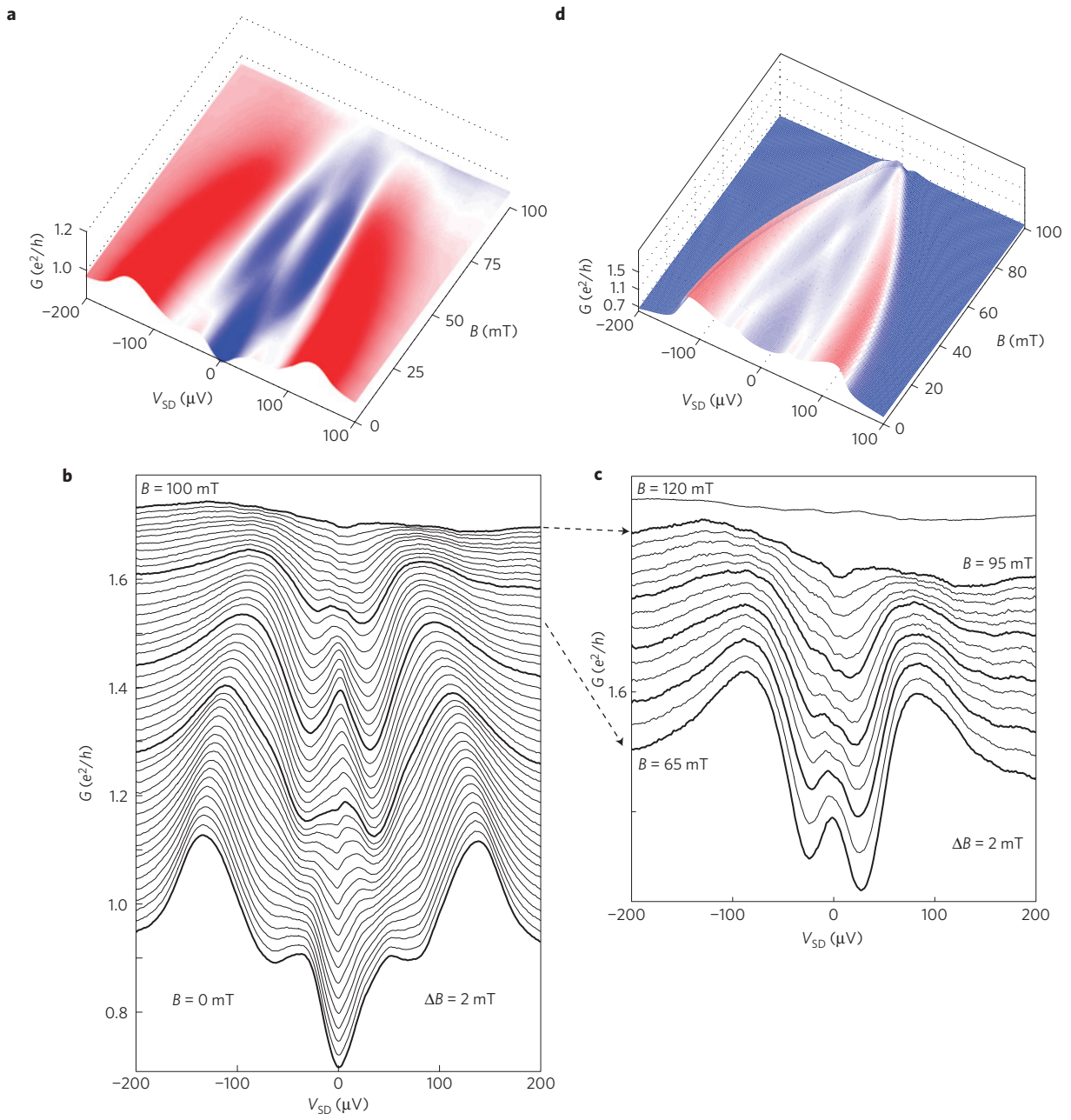

Figure 4 | Low-bias conductance as a function of applied magnetic field parallel to the wire axis (type II device, D4). a, Colour plot. **b**,**c**, Cuts in increments $\Delta B \sim 2$ mT (each shifted by $\sim 0.02e^2/h$). At $B = 0$, there is a typical conductance dip at $V_{SD} = 0$, flanked by two shoulders at $\pm eV_{SD} = \Delta_{ind} \sim 45\,\mu$V, and outer peaks at $\pm eV_{SD} = \Delta_{Al} \cong 150\,\mu$V. At $B \sim 30$ mT, the two shoulders merge into a single ZBP, and remain robust until ~70 mT. Beyond ~70 mT the ZBP splits and the conductance features are weaker. **c**, Zoom in of cuts between ~65–120 mT. The split peaks remain nearly parallel with increasing B. **d**, A simulation of the conductance with a topological segment length of 160 nm and spin–orbit energy of $\Delta_{so} = 70\,\mu$eV. A second channel was added in parallel, which ends with a Δ_{Al} superconductor, to account for the quasiparticles tunnelling into the aluminium at high energy (the contribution of this channel was ~75%, and that of the main channel was ~25%; see Supplementary Information). The measured dependence of Δ_{Al} and Δ_{ind} on the magnetic field was used. The data were convolved with a Fermi–Dirac kernel to simulate an electron temperature of 30 mK.

shoulders, which are a representation of the so-called induced gap in the nanowire. Determined by Cooper pairs tunnelling into the wire, this feature was found to be strongly dependent on the chemical potential in the wire, which in turn affected the wavefunction in the wire and consequently the tunnelling probability of the Cooper pairs. A typical value was $\Delta_{ind} \cong 50\,\mu$eV. The second feature, at higher bias, is two distinct peaks, being the representation of the bulk aluminium gap, $\Delta_{Al} \cong 150\,\mu$eV. The latter assignment was verified by carrying out a ~1 MHz shot noise measurement (type I device), revealing an abrupt change in the slope at $eV_{SD} = \Delta_{Al}$. For a transmission coefficient of the non-ideal aluminium–wire interface $t \sim 0.6$, current I and $T \sim 10$ mK, the measured noise spectral density agreed with the single-channel expression $S \sim 2e^*I(1-t^*)$, with $e^* = 2e$ and $t^* = t^2$ for $eV_{SD} < \Delta_{Al}$, and $e^* = e$ with $t^* = t$ for $eV_{SD} > \Delta_{Al}$ (ref. 29; Supplementary Fig. S5).

Characterization of the field emerging conductance peaks

The gold pedestal under the aluminium contact in type I devices fully screens the gate voltage, thus preventing tuning of the chemical

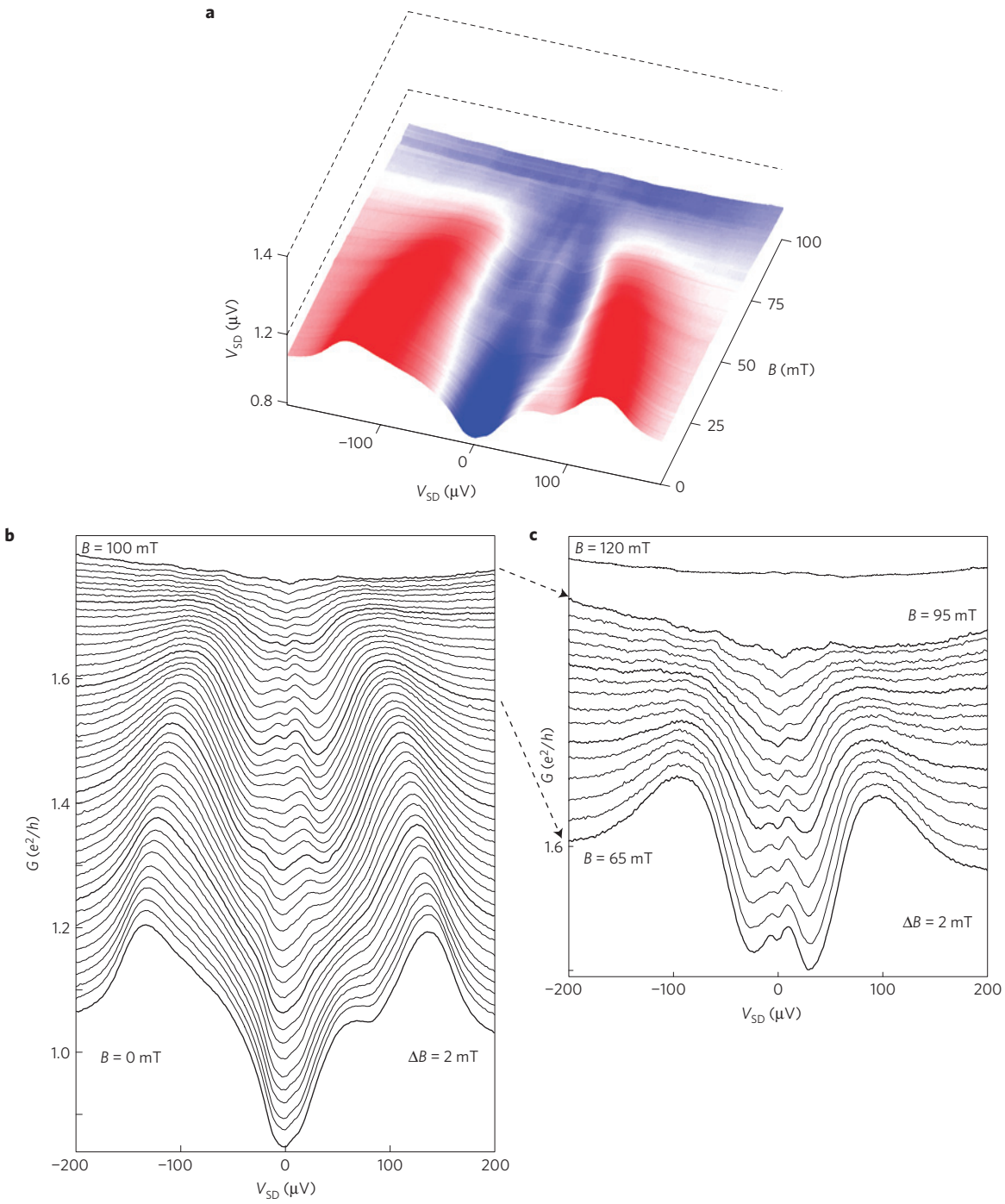

Figure 5 | Low-bias conductance as a function of applied magnetic field parallel to the wire axis (type II device, D4), at a higher chemical potential. a, 2D colour plot. **b**, Cuts with bias and magnetic field for $V_{RG} = 1.224$ V. The two shoulder peaks come closer with B but remain split and parallel to each other over a wide range of magnetic field (60–85 mT). They disappear when the Al superconductivity is quenched. **c**, Zoom in of the cuts in the interval 65–120 mT, allowing clear observation of the splitting.

potential under the aluminium contact. Indeed, none of the features observed in type II devices was also observed in two separate type I devices (D1 and D2).

Measurements were performed on two separate devices of type II (D3 and D4), and one of them was thermally cycled a few times. The differential conductance G_R was measured between the superconducting contact and the right contact, keeping the left side of the wire pinched-off. For a fixed global gate voltage, V_{GG}, the conductance fluctuated around constant values, exhibiting rather abrupt jumps at certain values of the local right gate voltage, V_{RG}—indicating an added subband transport. In the first subband, conductance diamonds were measured near the pinched-off regime, indicating distinct Coulomb blockade behaviour. At higher V_{RG}, a Kondo-correlated behaviour was apparent (with an odd–even effect), followed by Fabry–Perot oscillation with an average conductance of $G \sim 2e^2/h$ (ref. 44). The oscillation period corresponded approximately to 400 nm, which is of the order of the bare wire's segment length (reaffirming the dominant reflection from two weak barriers at the two end contacts—see Supplementary Information).

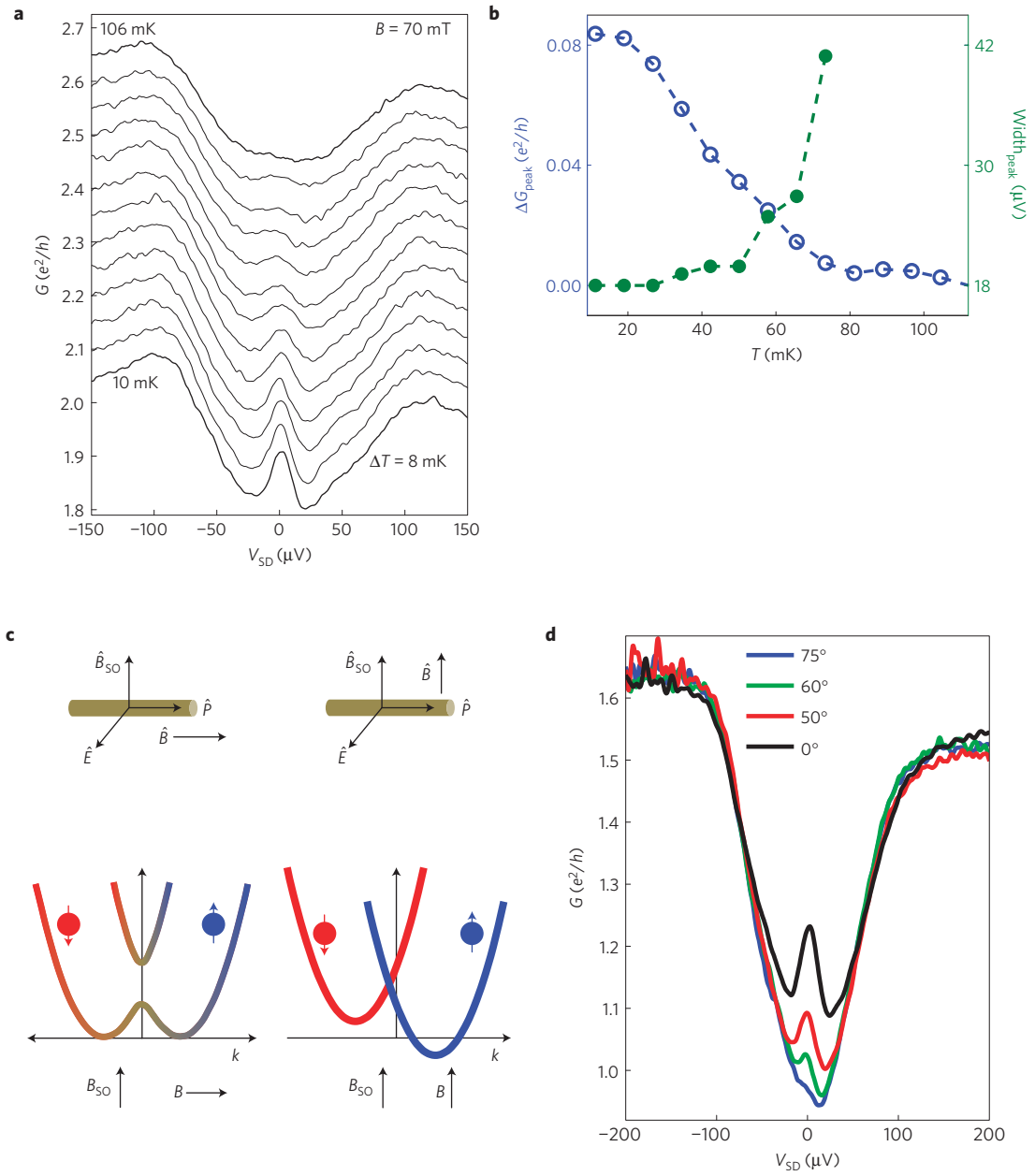

Figure 6 | Temperature and magnetic field orientation dependence of the ZBP of device D3 at $B = 70$ mT. a, Cuts at 8 mK intervals shifted by $0.05e^2/h$ each. The peak vanishes before $T \sim 100$ mK. **b**, Summary of the data. The estimated electron temperature is ~30 mK (dilution refrigerator temperature is 10 mK), leading to the observed peak width and lower conductance. **c**, Energy dispersion for the external field perpendicular to the spin-orbit effective field and parallel to it. **d**, Dependence of the ZBP on rotation angle, from 0° to 75°, where the peak practically vanishes, and back to 0°.

To locate an enhanced conductance at finite magnetic field near $V_{SD} = 0$, G_R was measured as a function of V_{RG} for different negative values of V_{GG} at zero and at ~50 mT. Such enhancement was found at sufficiently negative $V_{GG} = -15$ V to -18.5 V, and here we concentrate on data from device D4 (see Supplementary Fig. S10). We start with Fig. 3a, with the presented data measured at $V_{GG} = -18.3$ V and $V_{RG} = 1.17$–1.24 V, where V_{RG} controlled mainly the chemical potential in the wire segment under the superconductor. The zero-bias conductance in the left panel ($B = 0$), exhibits an obvious dip, flanked by the two induced gap shoulders at $\pm V_{SD} \sim 45\,\mu$V. At $B = 30$ mT and $V_{RG} = 1.205$ V (middle broken line), the two conductance shoulders near and turn into a relatively wide ZBP, which seems to barely split (a peak accompanied by a shoulder). At $V_{RG} = 1.183$ V the peak turns into two weak shoulders around $V_{SD} = 0$. Increasing the field to $B = 50$ mT, the ZBP is sharper, more distinct and persists for a wide range of gate voltage ($G_{peak} \cong 0.1e^2/h$; width $\sim 18\,\mu$V—agreeing with electron temperature of 30 mK). Splitting is obvious at high and low gate voltages. At $B = 70$ mT (approaching the superconducting critical field of 100 mT), the conductance features get weaker, with persistent split peaks (see Supplementary Fig. S10). The results are concisely summarized in the colour plot in Fig. 3b, where the peak height of the ZBP is plotted as a function of V_{RG} and B (after background subtraction). Each contour line indicates an equal ZBP height, where the three arrows indicate the region of transition between a single ZBP and split peaks.

As this is an essential point, we discuss it further. We have shown in the section addressing theoretical aspects that the wire enters the topological phase for $E_Z > \Delta_{ind}$, but only within $\Delta\mu = 2\sqrt{E_Z^2 - \Delta_{ind}^2}$. When μ is close to one of its topological

limits, the topological gap E_g is small and the overlap between the Majorana wavefunctions (with an extent $\xi \approx (\hbar v_F/E_g)$, where v_F is the Fermi velocity) causes the splitting of the ZBP. Alternatively, a single ZBP suggests a large gap E_g. Whereas at small B the relevant gap $E_g(0)$ is sensitive to μ, at high B the relevant gap is $E_g(p_F)$, which is only moderately affected by μ. Figure 3b describes this dependence, where the ZBP contours open up with increasing field resembling a square root dependence, later to diminish rather abruptly around 70 mT (at higher field the ZBP always splits)—mostly owing to the shrinking of the superconducting gap with field. Figure 3c shows the results of a theoretical analysis for three ZBP contours (calculated for an infinite wire), corresponding to different wavefunction extents, in terms of a topological superconductor segment length $L = 150$ nm. These contours resemble closely the experimental ones. The rigidity of the ZBP was also tested as a function of V_{GG} in Supplementary Fig. S11.

We now explore the evolution of the ZBP and its splitting with magnetic field in three regimes of the chemical potential. We start with $\mu \sim 0$ ($V_{RG} = 1.205\,V$ in Fig. 3a), presented in Fig. 4a–c. The two inner shoulders (associated with $\Delta_{ind} \sim 45\,\mu$eV at $B = 0$) merge into a ZBP at $B \sim 35$ mT. Beyond $B \sim 70$ mT, the ZBP splits; however, rather weakly. It is important to note that these low-bias conductance features disappear when the superconducting gap collapses at $B \sim 100$ mT. As shown in Fig. 3, gap closing and split Majorana peaks evolve together at the low-field regime ($B = 30$–35 mT). At high field, the splitting is expected to result owing to gap closing at the Fermi momentum $E_g(p_F)$. Detailed numerical simulations were performed for a single subband wire, where many of the system parameters were taken into account (except for disorder, as described in the Supplementary Information). With spin–orbit energy $\Delta_{so} \sim 70\,\mu$eV (reported values are $\lambda_{so} \approx 127$ nm with $\Delta_{so} \approx 75\,\mu$eV (refs 45,46) for $m^* = 0.03m_e$ and $v_F \propto \sqrt{2\Delta_{so}/m^*}$, leading to $\xi \approx (\hbar v_F/E_g) \sim 270$ nm for maximal value of $E_g = 70\,\mu$eV), and distance $L \approx 160$ nm between the two Majoranas, we find a rather good agreement with the data (Fig. 4a,d). Note that the oscillation of the Majorana wavefunction[9] with a typical length of order $\lambda_F \approx \lambda_{so}$ enables a small overlap between the Majoranas and hence a small ZBP splitting even when $\xi \approx L$, see also Supplementary Fig. S1.

For the chemical potential in its high end, $V_{RG} = 1.224$ V (Fig. 3a), the topological gap is expected to be smaller, thus enhancing the splitting of the ZBP. Indeed, the colour scale and the corresponding cuts in Fig. 5 show such a dependence on field. The split peaks stay nearly parallel with B, disappearing together with the superconducting gap. Similar behaviour was observed with the chemical potential near its lowest border (see Supplementary Fig. S13). Note that the closing of the gap with field is not always evident in the data (Supplementary Fig. S14). Our simulation shows that the strength of the peaks associated with closing of the gap depends on details such as the barrier height (Supplementary Fig. S2).

The validity of assigning the ZBP to the Majorana can be further tested through the sensitivity of the conductance to the temperature and the orientation of the magnetic field. The temperature dependence of the ZBP was measured at $B = 70$ mT in the type II device; as shown in Fig. 6a,b (the D3 device had a higher critical field of ~150 mT). The peak height ΔG_{max} and width are plotted as a function of the lattice temperature (Fig. 6b). Although the expected theoretical height is $2e^2/h$, the lower observed value could be related to: coupling between the Majorana fermions[47], temperature quenching $G_{max} \propto \Gamma/T_e$ (Γ—natural energy broadening of the ZBP) and broadening $3.5k_BT \cong 9\,\mu$eV. The ZBP width seems indeed to provide a reasonable measure of the electron temperature T_e; namely, at a lattice temperature of ~10 mK, the measured peak width led to $T_e \sim 30$ mK. Although the peak height and width lag at the lowest temperature, which is reasonable; a crude estimate of the natural broadening leads to $\Gamma \sim 1\,\mu$eV.

The topological gap opens up when the external field is perpendicular to the spin–orbit field. To test this dependence, a type II device (D3) was placed on a piezoelectric rotator (Autocube # ANR220\RES) and the ZBP was measured for a few angles of the field in the wire–spin–orbit plane (0° is along the nanowire). As seen in Fig. 6c,d, the ZBP nearly disappeared at 75°.

Discussion

The characteristics of the near-zero-energy conductance of the composite InAs nanowire–aluminium superconductor seem to agree with the formation of Majorana states; however, competitive mechanisms may also leave similar fingerprints. The following support the Majorana picture: ZBP was not found in type I devices (D1 and D2), where the chemical potential in the wire segment beneath the Al was fixed; the ZBP robustly appeared in a limited range of the chemical potential; the ZBP appeared only in the presence of a topological gap, namely, $E_Z > \Delta_{ind}$; ZBP splitting is correlated with a small topological gap—controlled by the chemical potential and the field; the ZBP vanished at ~100 mK; the ZBP disappeared following rotation of the field towards the spin–orbit field; numerical simulations of the Majorana scenario with reasonable parameters reproduce the observed results. On the other hand, we did not observe the splitting energy of the ZBP oscillating with the chemical potential (the magnetic field range might be too small for such observation). Needless to say that further studies, such as observing a quantum conductance of $2e^2/h$, a non-local Josephson effect[48] and shot noise experiments[49], are desired.

We end by mentioning a few proposed scenarios that may lead to similar conductance features. Note that to be serious candidates for the observed ZBP and its splitting, they must account for all of the above features supporting the Majorana picture. Among a growing number of counter proposals, a few are worth mentioning. The first one is weak anti-localization[42]. It is mainly a multi-channel effect, but the normal wire is likely to have a single channel. The second proposal is the conventional Kondo effect. It is likely that the wire does not support Kondo correlations: the normal segment, tuned to a highly conductive Fabry–Perot oscillation regime, does not show any sign of a charging effect (see Supplementary Fig. S15), or any even–odd effects, and the superconducting segment, contacted by an infinitely large superconductor, is thus void of charging energy. Moreover, Zeeman splitting should be observed (even for $g \sim 2$), and a ZBP is absent when the superconductor gap quenches. The third proposal is finite-energy Andreev bound states. They may mimic the observed splitting[50], only for an extremely small g-factor ($g \sim 2$). The fourth proposal is localized clusters of low-energy states. Such localized states near the wire's end below the superconductor[22] are likely to appear for sizable disorder and multiple channels. On the contrary, the Fabry–Perot oscillations suggest that the elastic mean free path is longer than the wire length[44].

Received 30 July 2012; accepted 10 October 2012; published online 11 November 2012

References

1. Dirac, P. A. M. Quantum mechanics of many-electron systems. *Proc. R. Soc. Lond. Ser. A* **123,** 714–733 (1929).
2. Majorana, E. Teoria simmetrica dell elettronee del positrone. *Il Nuovo Cimento (1924-1942)* **14,** 171–184 (1937).
3. Wilczek, F. Majorana returns. *Nature Phys.* **5,** 614–618 (2009).
4. Kitaev, A. Y. Unpaired Majorana fermions in quantum wires. *Phys.-Usp.* **44,** 131–136 (2001).
5. Kopnin, N. & Salomaa, M. Mutual friction in superfluid ^{3}He: Effects of bound states in the vortex core. *Phys. Rev. B* **44,** 9667–9677 (1991).
6. Alicea, J. New directions in the pursuit of Majorana fermions in solid state systems. *Rep. Prog. Phys.* **75,** 076501 (2012).
7. Beenakker, C. Search for Majorana fermions in superconductors. Preprint at http://arxiv.org/abs/1112.1950 (2011).

8. Kitaev, A. Y. Fault-tolerant quantum computation by anyons. *Ann. Phys.* **303,** 2–30 (2003).
9. Halperin, B. I. *et al.* Adiabatic manipulations of Majorana fermions in a three-dimensional network of quantum wires. *Phys. Rev. B* **85,** 144501 (2012).
10. Sau, J. D., Clarke, D. J. & Tewari, S. Controlling non-Abelian statistics of Majorana fermions in semiconductor nanowires. *Phys. Rev. B* **84,** 094505 (2011).
11. Read, N. & Green, D. Paired states of fermions in two dimensions with breaking of parity and time-reversal symmetries and the fractional quantum Hall effect. *Phys. Rev. B* **61,** 10267 (2000).
12. Kitaev, A. Anyons in an exactly solved model and beyond. *Ann. Phys.* **321,** 2–111 (2006).
13. Alicea, J., Oreg, Y., Refael, G., Oppen, F. V. & Fisher, M. P. A. Non-Abelian statistics and topological quantum information processing in 1D wire networks. *Nature Phys.* **7,** 412–417 (2011).
14. Fu, L. & Kane, C. L. Superconducting proximity effect and Majorana fermions at the surface of a topological insulator. *Phys. Rev. Lett.* **100,** 96407 (2008).
15. Sau, J. D., Lutchyn, R. M., Tewari, S. & Sarma, S. D. Generic new platform for topological quantum computation using semiconductor heterostructures. *Phys. Rev. Lett.* **104,** 40502 (2010).
16. Sau, J., Tewari, S., Lutchyn, R. & Stanescu, T. Non-Abelian quantum order in spin-orbit-coupled semiconductors: Search for topological Majorana particles in solid-state systems. *Phys. Rev. B* **82,** 1–59 (2010).
17. Alicea, J. Majorana fermions in a tunable semiconductor device. *Phys. Rev. B* **81,** 125318 (2010).
18. Lutchyn, R. M., Sau, J. D. & Sarma, S. D. Majorana fermions and a topological phase transition in semiconductor-superconductor heterostructures. *Phys. Rev. Lett.* **105,** 77001 (2010).
19. Oreg, Y., Refael, G. & Oppen, F. V. Helical liquids and Majorana bound states in quantum wires. *Phys. Rev. Lett.* **105,** 177002 (2010).
20. Mourik, V. *et al.* Signatures of Majorana fermions in hybrid superconductor-semiconductor nanowire devices. *Science* **336,** 1003–1007 (2012).
21. Deng, M. T. *et al.* Observation of majorana fermions in a Nb–InSb nanowire-Nb hybrid quantum device. Preprint at http://arxiv.org/abs/1204.4130 (2012).
22. Potter, A. C. & Lee, P. A. Multichannel generalization of Kitaev's Majorana end states and a practical route to realize them in thin films. *Phys. Rev. Lett.* **105,** 227003 (2010).
23. Pientka, F., Kells, G., Romito, A., Brouwer, P. W. & von Oppen, F. Enhanced zero-bias Majorana peak in disordered multi-subband quantum wires. Preprint at http://arxiv.org/abs/1206.0723 (2012).
24. Rainis, D., Trifunovic, L., Klinovajo, J. & Loss, D. Realistic transport modeling for a superconducting nanowire with Majorana fermions. Preprint at http://arxiv.org/abs/1207.5907v1 (2012).
25. Bychkov, Y. A. & Rashba, E. Oscillatory effects and the magnetic susceptibility of carriers in inversion layers. *J. Phys. C* **17,** 6039–6045 (1984).
26. Wimmer, M., Akhmerov, A., Dahlhaus, J. & Beenakker, C. Quantum point contact as a probe of a topological superconductor. *New J. Phys.* **13,** 053016 (2011).
27. Bolech, C. & Demler, E. Observing majorana bound states in *p*-wave superconductors using noise measurements in tunneling experiments. *Phys. Rev. Lett.* **98,** 237002 (2007).
28. Shtrikman, H., Popovitz-Biro, R., Kretinin, A. V. & Kacman, P. GaAs and InAs nanowires for ballistic transport. *IEEE J. Selected Top. Quant. Electron.* **17,** 922–934 (2011).
29. Das, A. *et al.* Entangling electrons by splitting Cooper pairs: Two-particle conductance resonance and time coincidence measurements. Preprint at http://arxiv.org/abs/1205.2455 (2012).
30. Blonder, G., Tinkham, M. & Klapwijk, T. Transition from metallic to tunneling regimes in superconducting microconstrictions: Excess current, charge imbalance, and supercurrent conversion. *Phys. Rev. B* **25,** 4515–4532 (1982).
31. Lin, C. H., Sau, J. D. & Sarma, S. D. Zero bias conductance peak in Majorana wires made of semiconductor-superconductor hybrid structures. Preprint at http://arxiv.org/abs/1204.3085 (2012).
32. Qu, C., Zhang, Y., Mao, L. & Zhang, C. Signature of majorana fermions in charge transport in semiconductor nanowires. Preprint at http://arxiv.org/abs/1109.4108 (2011).
33. Stanescu, T. D., Lutchyn, R. M. & Sarma, S. D. Majorana fermions in semiconductor nanowires. *Phys. Rev. B* **84,** 144522 (2011).
34. Prada, E., San-Jose, P. & Aguado, R. Transport spectroscopy of NS nanowire junctions with Majorana fermions. Preprint at http://arxiv.org/abs/1203.4488 (2012).
35. Andreev, A. Thermal conductivity of superconductors intermediate state. *Soviet Phys. ZhETP* **46,** 1823–1828 (1964).
36. Marmorkos, I., Beenakker, C. & Jalabert, R. Three signatures of phase-coherent Andreev reflection. *Phys. Rev. B* **48,** 2811–2814 (1993).
37. Kastalsky, A. *et al.* Observation of pair currents in superconductor-semiconductor contacts. *Phys. Rev. Lett.* **67,** 3026–3029 (1991).
38. Pillet, J. *et al.* Andreev bound states in supercurrent-carrying carbon nanotubes revealed. *Nature Phys.* **6,** 965–969 (2010).
39. Klapwijk, T., Blonder, G. & Tinkham, M. Explanation of subharmonic energy gap structure in superconducting contacts. *Physica B + C* **109,** 1657–1664 (1982).
40. Goldhaber-Gordon, D. *et al.* Kondo effect in a single-electron transistor. *Nature* **391,** 156–159 (1998).
41. Kretinin, A. V. *et al.* Spin-1/2 Kondo effect in an InAs nanowire quantum dot: Unitary limit, conductance scaling, and Zeeman splitting. *Phys. Rev. B* **84,** 245316 (2011).
42. Pikulin, D., Dahlhaus, J., Wimmer, M. & Beenakker, C. Zero-voltage conductance peak from weak antilocalization in a Majorana nanowire. Preprint at http://arxiv.org/abs/1206.6687 (2012).
43. Csonka, S. *et al.* Giant fluctuations and gate control of the g-factor in InAs nanowire quantum dots. *Nano Lett.* **8,** 3932–3935 (2008).
44. Kretinin, A. V., Popovitz-Biro, R., Mahalu, D. & Shtrikman, H. Multimode Fabry–Perot conductance oscillations in suspended stacking-faults-free InAs nanowires. *Nano Lett.* **10,** 3439–3445 (2010).
45. Fasth, C., Fuhrer, A., Samuelson, L., Golovach, V. N. & Loss, D. Direct measurement of the spin-orbit interaction in a two-electron InAs nanowire quantum dot. *Phys. Rev. Lett.* **98,** 266801 (2007).
46. Kanai, Y. *et al.* Electrically tuned spin-orbit interaction in an InAs self-assembled quantum dot. *Nature Nanotech.* **6,** 511–516 (2011).
47. Fu, L. Electron teleportation via Majorana bound states in a mesoscopic superconductor. *Phys. Rev. Lett.* **104,** 56402 (2010).
48. Jiang, L. *et al.* Unconventional Josephson signatures of Majorana bound states. *Phys. Rev. Lett.* **107,** 236401 (2011).
49. Nilsson, J., Akhmerov, A. & Beenakker, C. Splitting of a Cooper pair by a pair of Majorana bound states. *Phys. Rev. Lett.* **101,** 120403 (2008).
50. Chevallier, D., Sticlet, D., Simon, P. & Bena, C. Mutation of Andreev into Majorana bound states in long superconductor-normal and superconductor-normal-superconductor junctions. *Phys. Rev. B* **85,** 235307 (2012).

Acknowledgements

We thank A. Haim, A. Stern, F. von Oppen and G. Refael for useful discussions. We are grateful to R. Popovitz-Biro and D. Mahalu for their professional contribution and to A. Kretinin for laying the groundwork for nanowire device physics, and S. Ilani and A. Joshua for enabling us to perform the tilted field measurement. M.H. acknowledges the partial support of the Israeli Science Foundation (ISF), the Minerva foundation, the US-Israel Bi-National Science Foundation (BSF) and the European Research Council under the European Community's Seventh Framework Program (FP7/2007-2013)/ERC Grant agreement # 227716. Y.O. acknowledges the partial support of the DFG, Minerva and that of the BSF. H.S. acknowledges the partial support of the ISF and the Israeli Ministry of Science and Technology (IMOST).

Author contributions

A.D. and Y.R. contributed to sample design, device fabrication, set-up, data acquisition, analysis and writing of the paper. M.H. contributed to design, data interpretation and writing of the paper. Y.M. contributed to theory, simulations and writing of the paper. Y.O. contributed to theory, simulations, experimental insight and writing of the paper. H.S contributed to the Au-assisted vapour-liquid–solid molecular beam epitaxy growth and structural study of InAs nanowires, discussions and editing of the manuscript.

Additional information

Supplementary information is available in the online version of the paper. Reprints and permissions information is available online at www.nature.com/reprints. Correspondence and requests for materials should be addressed to M.H.

Competing financial interests

The authors declare no competing financial interests.